Met. Mater. Int., Vol. 23, No. 6 (2017), pp. 1241~1249
doi: 10.1007/s12540-017-7105-y

High Performance Sb_2S_3/Carbon Composite With Tailored Artificial Interface as an Anode Material for Sodium Ion Batteries

Jeong-Hee Choi[1,2], Chung-Wan Ha[1], Hae-Young Choi[1], Heon-Cheol Shin[2,*], and Sang-Min Lee[1,*]

[1]Battery Research Center, Korea Electrotechnology Research Institute, Changwon 51543, Republic of Korea
[2]School of Materials Science and Engineering, Pusan National University, Busan 46241, Republic of Korea

(received date: 8 February 2017 / accepted date: 3 April 2017)

The electrochemical comparison between Sb_2S_3 and its composite with carbon (Sb_2S_3/C) involved by sodium ion carrier are explained by enhanced kinetics, particularly with respect to improved interfacial conductivity by surface modulation by carbon. Sb_2S_3 and Sb_2S_3/C are synthesized by a high energy mechanical milling process. The successful synthesis of these materials is confirmed with X-ray diffraction (XRD), scanning electron microscopy, and transmission electron microscopy (TEM). As an anode material for sodium ion batteries, Sb_2S_3 exhibits an initial sodiation/desodiation capacity of 1,021/523 mAh g^{-1} whereas the Sb_2S_3/C composite exhibits a higher reversible capacity (642 mAh g^{-1}). Furthermore, the cycle performance and rate capability of the Sb_2S_3/C composite are estimated to be much better than those of Sb and Sb_2S_3. Electrochemical impedance spectroscopy analysis shows that the Sb_2S_3/C composite exhibited charge transfer resistance and surface film resistance much lower than Sb_2S_3. X-ray photoelectron spectroscopy analyses of both electrodes demonstrate that NaF layer on Sb_2S_3/C composite electrode leads to the better electrochemical performances. In order to clarify the electrochemical reaction mechanism, ex-situ XRD based on differential capacity plots and ex-situ HR-TEM analyses of the Sb_2S_3/C composite electrode are carried out and its reaction mechanism was established.

Keywords: energy storage materials, intermetallics, composites, mechanical alloying/milling, electrochemistry

1. INTRODUCTION

Lithium ion batteries (LIBs) have been established for several decades as essential components of portable electronic devices because they deliver higher energy densities and better durability than other rechargeable batteries [1-3]. The demand for appropriate power sources is increasing accordingly [4]. Recently, smart grids and energy storage systems (ESSs) have been proposed with the aim of optimizing energy efficiency. In addition, electric vehicles (EVs) and hybrid electric vehicles (HEVs) are expected to provide the next generation of automobiles that will replace conventional cars with combustion engines. Thus rechargeable batteries are required not only for small applications such as mobile devices, but also for large systems such as ESSs and EVs [1,3-5]. LIBs are recognized as the best battery systems for large scale applications because of their high energy densities and long durability in commercialization stage [4,6-8]. However, lithium resources are concentrated in only a few regions of the world, and the demand for lithium is expected to increase sharply [9-12]. Consequently, there are concerns that the balance between the demand for and supply of lithium will be lost, and that as a result the cost of lithium will increase. Therefore, a new battery concept that can supply the energy density and long-term durability of LIB batteries but that does not have the same resource concerns is needed.

Sodium ion batteries (NIBs) have the potential to meet these requirements because of the chemical similarity of sodium and lithium [13-15]. Although the cathode materials for NIBs, like those of their lithium analogues, exhibit satisfactory electrochemical performances [13,16], the development of anode materials for NIBs remains a significant challenge because the use of graphite as the anode in NIBs has not resulted in electrochemical performances equivalent to those of LIBs [17]. Hard carbon is an alternative to graphite that has been demonstrated to exhibit acceptable electrochemical performances and good reversibility as an anode material in NIBs. However, its available capacity is limited (< 300 mAh g^{-1}) and its reaction potential near Na plating gives rise to serious safety concerns [14,15]. Na-alloying elements such as Sn, P, Ge, Sb, and Pb have been suggested as possible solutions to these issues of carbonaceous materials including hard carbon [14,15,18]. However, these materials undergo electrode degradation during

*Corresponding authors: hcshin@pusan.ac.kr, sangma@keri.re.kr

the large volume expansions that arise in sodiation/desodiation processes [19]. Sb has received particular attention as a promising alloy anode material for NIBs because of its large capacity and low atomic packing factor (~39%) resulting in having more space to accommodate Na ion than other alloy elements [14]. Furthermore, it shows little negative influences such as the decrease of initial coulombic efficiency (ICE) and the increase of reaction resistance by fluoroethylene carbonate (FEC) additive forming the stable solid electrolyte interface (SEI) [6,14,20]. To overcome the large volume expansion (390%) of Sb, various methods such as the preparation of composites with carbon [21,22], structures alleviating volume expansion [23-25], and intermetallic compounds have been suggested. Sb_2S_3 is noteworthy because its theoretical capacity is 946 mAh g^{-1}, which is higher than the capacity of Sb. Flower-like Sb_2S_3 have been shown to exhibit high capacities and good electrochemical performances as anode materials [26]. In particular, the bulky modification such as Sb_2S_3 seeks for alleviating the grain expansion of Na_xSb surrounded by Na-S matrix phase. However, the only bulky modification is not sufficient for controlling the side reaction at interface between electrolyte and anode surface with full sodiation.

In this work, carbonaceous surface on Sb_2S_3 is intentionally designed to enhance interfacial conductivity through stable passivating film. The carbonaceous surface is hypothesized to be more stable to carbonate based electrolyte than metallic surface which is known to be less passivated. We develop a simple and facile method of high energy mechanical milling (HEMM) for the preparation of Sb_2S_3 and Sb_2S_3/C nanocomposites without any further processing and evaluate them as anode materials for NIBs. Their electrochemical performances including capacity, cycle life, and rate capability are assessed. Furthermore, the sodiation/desodiation reaction mechanism of the as-synthesized Sb_2S_3/C nanocomposite, which exhibits superior electrochemical performance, is suggested by using ex-situ XRD analysis of the electrode at several reaction potentials in the first cycle based on differential capacity plots (DCPs). Additionally, HR-TEM analyses at fully sodiated and desodiated Sb_2S_3/C composite are also conducted for suggesting its reaction mechanism.

2. EXPERIMENTAL PROCEDURE

2.1. Syntheses of Sb_2S_3 and the Sb_2S_3/C composite

Sb_2S_3 and its composite with carbon are prepared with solid-state processes. Sb_2S_3 is synthesized through the high energy mechanical milling (HEMM, Pluretes-5) of stoichiometric amounts of Sb (Aldrich, 99%, -100 Mesh) and S (Aldrich, 99%, -100 Mesh) powders for 12 hours at 300 rpm under an Ar atmosphere. The as-synthesized Sb_2S_3 powders, super P, and zirconia balls (diameter : Ø5) with a ball to powder ratio of 20:1 by weight are placed into a 80 mL-zirconia vial. The amounts of Sb_2S_3 and super P were 70% and 30% by weight respectively. The additional HEMM process for obtaining the Sb_2S_3/C composite is conducted for 3 hours.

2.2. Material characterizations

The Sb_2S_3 and Sb_2S_3/C composite samples are characterized by using X-ray diffraction (XRD, Philips, X'Pert Pro MPD), field-emission scanning electron microscopy (FE-SEM, HITACHI S-4800) combined with energy-dispersive spectroscopy (EDS), and high resolution transmission electron microscopy (HR-TEM, FEI Titan G2 ChemiSTEM Cs probe) operated at 200 kV. Ex-situ XRD study of Sb_2S_3/C composite electrode is conducted to observe the structural changes at several sodiation/desodiation potentials. For observing the microstructural changes at sodiated and desodiated Sb_2S_3/C electrode, HR-TEM analysis is conducted on the collected powders from the fully sodiated and desodiated electrode. X-ray photoelectron spectroscopy (XPS, Thermo Scientific, Multilab 2000) is used for identifying the surface film formed on the electrodes.

2.3. Electrochemical measurements

For each electrochemical evaluation of Sb_2S_3 and Sb_2S_3/C composite, the electrodes are fabricated by coating the slurry consisting of active material (70 wt%), Super P as conducting agent (15 wt%), and polyacrylic acid (PAA, 15 wt%) dissolved in N-methyl pyrrolidinone (NMP) as the binder onto a copper foil substrate with a thickness of 11 μm. The as-fabricated electrodes were dried overnight at 120 °C in a vacuum oven. The mass loading of the electrodes is approximately 3-4 mg cm^{-2}. 2032 coin-type electrochemical cells were assembled in an Ar-filled glove box with a 200 μm glass microporous fiber (GMF) as the separator, Na metal as the counter and reference electrodes, and 1 M $NaClO_4$ in an ethylene carbonate (EC)/propylene carbonate (PC) (1:1 by volume) electrolyte solution containing 5 wt% fluoroethylene carbonate (FEC) (Panax Etec Co., Ltd., Korea). All the cells including cycling performances and rate capabilities are tested galvanostatically between 0.005 V and 2.0 V (vs. Na/Na^+) at various current densities (50-2,000 mA g^{-1}) by using a Maccor tester (Series 4600A) at room temperature. Electrochemical impedance spectroscopy (EIS) was conducted with a frequency response analyzer (Biologic, VMP3) at frequencies ranging from 1 MHz to 10 mHz with an amplitude voltage of 5 mV.

3. RESULTS AND DISCUSSION

Figure 1 shows the XRD patterns of the Sb_2S_3 and Sb_2S_3/C composite samples synthesized by HEMM. All the peaks in the XRD pattern of the Sb_2S_3 sample match those of the Sb_2S_3 phase (JCPDS 42-1393) exactly, whereas the Sb_2S_3/C composite has lower crystallinity than Sb_2S_3, as is evident in the broader peaks in its XRD pattern, which are due to the additional mechanical milling with carbon. No peaks corresponding to the residual starting elements Sb or S can be seen. The

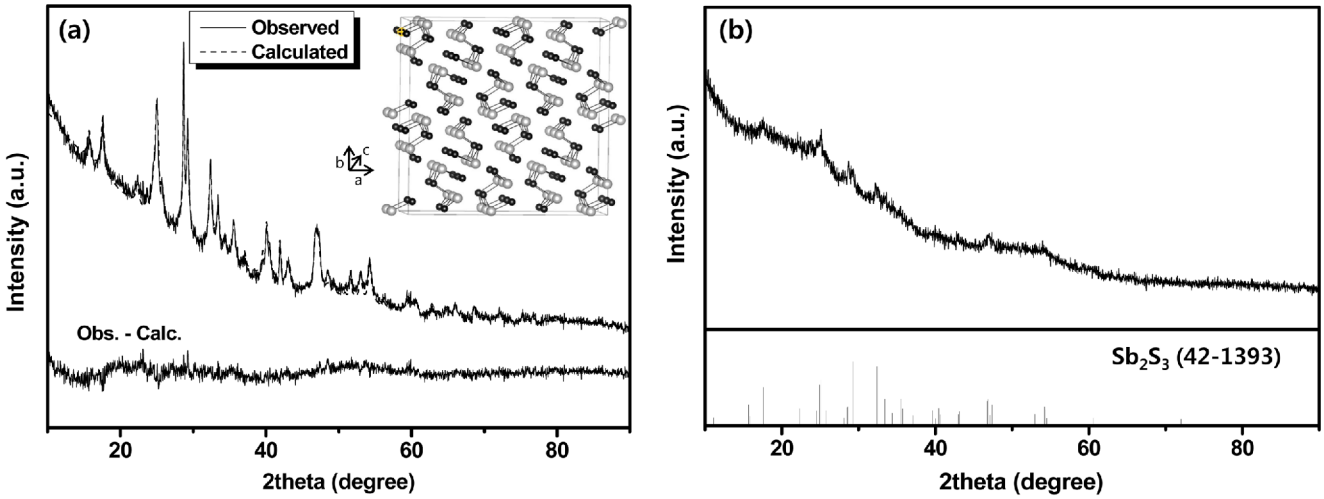

Fig. 1. XRD patterns collected from (a) Sb_2S_3 (inset: crystalline structure of Sb_2S_3, gray : S, black : Sb) and (b) Sb_2S_3/C composite.

inset in Fig. 1 shows the crystalline structure of intermetallic Sb_2S_3 (orthorhombic, space group: Pbnm, a = 11.307 Å, b = 11.235 Å, c = 3.842 Å). The lattice parameters of the Sb_2S_3 sample are obtained by using Rietveld refinement. Rietveld refinement of the XRD patterns obtained from Sb_2S_3 reveals that the experimental pattern agrees well with the simulated results. Therefore, the HEMM process is an effective method for the synthesis of Sb_2S_3 and its composite with carbon. The morphologies and elemental analysis of the as-synthesized Sb_2S_3 and Sb_2S_3/C composite samples are characterized by using SEM and EDX analysis. Figures 2(a) and 2(b) show that Sb_2S_3 particles with diameters of several micrometers are present and that elemental Sb and S are distributed homogeneously within the particles. As displayed in Fig. 2(c), the HR-TEM image and its Fourier transform (FT) reveal that the Sb_2S_3 phase produces three groups of distinctive lattice fringes, which are

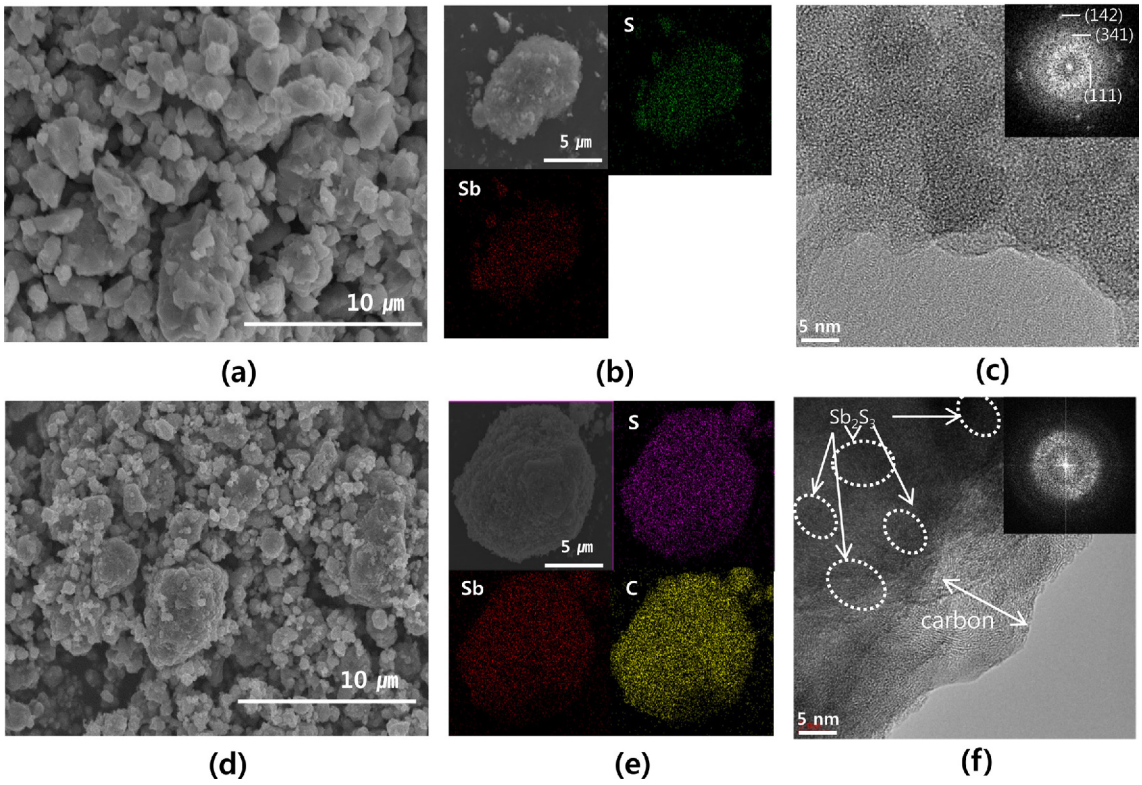

Fig. 2. Sb_2S_3; (a) SEM image, (b) EDS mapping, and (c) HR-TEM image. Sb_2S_3/C composite; (d) SEM image, (e) EDS mapping, and (f) HR-TEM image.

due to the high crystallinity of the sample. In the case of the Sb_2S_3/C composite, primary particles with sizes of hundreds of nm have aggregated to form secondary particles with sizes of several micrometers in which elemental Sb, S, and carbon are distributed homogeneously (Figs. 2(d) and 2(e)). As shown in Fig. 2(f), Sb_2S_3 becomes amorphous in the Sb_2S_3/C composite due to the additional milling with carbon. Sb_2S_3 nanocrystallites with an approximate size of 5-10 nm are covered by the amorphous carbon layer.

The electrochemical performances of Sb_2S_3 and its carbon composite form are tested in the 2032 coin half cell. Figure 3(a) shows the initial voltage profiles of the Sb_2S_3 and Sb_2S_3/C composite samples at 50 mA g^{-1}. During the initial sodiation step, Sb_2S_3 exhibits a larger capacity (1,031 mAh g^{-1}) than the Sb_2S_3/C composite (826 mAh g^{-1}) by approximately 200 mAh g^{-1}. However, the desodiation capacity of Sb_2S_3 (523 mAh g^{-1}) is lower than that of its composite form (642 mAh g^{-1}) by approximately 120 mAh g^{-1}. Since the electrode conductivity and structural stability of Sb_2S_3/C become better by forming composite with carbon, the initial irreversible reaction including SEI formation is considered to be reduced and thereby, its electrochemical reversibility with Na is improved remarkably. This high desodiation capacity of the Sb_2S_3/C composite exceeds that of the Sb/C composite (610 mAh g^{-1}) which is calculated on the basis of only Sb mass [21]. In addition, the Sb_2S_3/C composite exhibits lower reaction resistance than Sb_2S_3 because the Sb_2S_3/C composite exhibits lower polarization than Sb_2S_3 during the sodiation and desodiation steps. This result indicates that the Sb_2S_3/C composite exhibits better electrochemical reversibility than Sb_2S_3 because of the carbon conductive network. As a result, the initial coulombic efficiency of the Sb_2S_3/C composite, 78%, is much higher than that of Sb_2S_3 (51%). This high ICE value is higher than those reported for a Sb_2S_3 nanoparticle-decorated graphene composite (69%) and flower-like Sb_2S_3 (73%), although its initial desodiation capacity is a little lower than obtained in these previous studies [26,27]. In addition, the Sb_2S_3/C composite is more easily synthesized by HEMM, requiring only one or two steps without further treatments, than by other processes. Figure 3(c) shows the rate capabilities of Sb_2S_3 and its composite with carbon. The electrodes were sodiated and desodiated for 5 cycles at various current densities, 50, 200, 500, 1000, and 2000 mA g^{-1}. After conducting the rate capability tests at the highest current density (2000 mA g^{-1}) for 5 cycles, the electrodes were tested again under the initial conditions (50 mA g^{-1}) to assess their structural stabilities. The Sb_2S_3/C composite electrode delivers high desodiation capacities of 598 mAh g^{-1}, 579 mAh g^{-1}, and 557 mAh g^{-1} at the higher current densities 200, 500, and 1000 mA g^{-1} respectively. When current density increased to 2000 mA g^{-1} finally corresponding to 3C rate, a desodiation capacity of 520 mAh g^{-1}, which is equivalent to 80% of the capacity at 50 mA g^{-1}, was achieved. This remarkable rate capability demonstrates that at high current densities this composite permits Na ions and electrons to transport reversibly during the sodiation/desodiation reaction. When the current density was reduced to 50 mA g^{-1} again after testing at 2,000 mA g^{-1}, the capacity of the electrode almost completely recovered to its initial capacity.

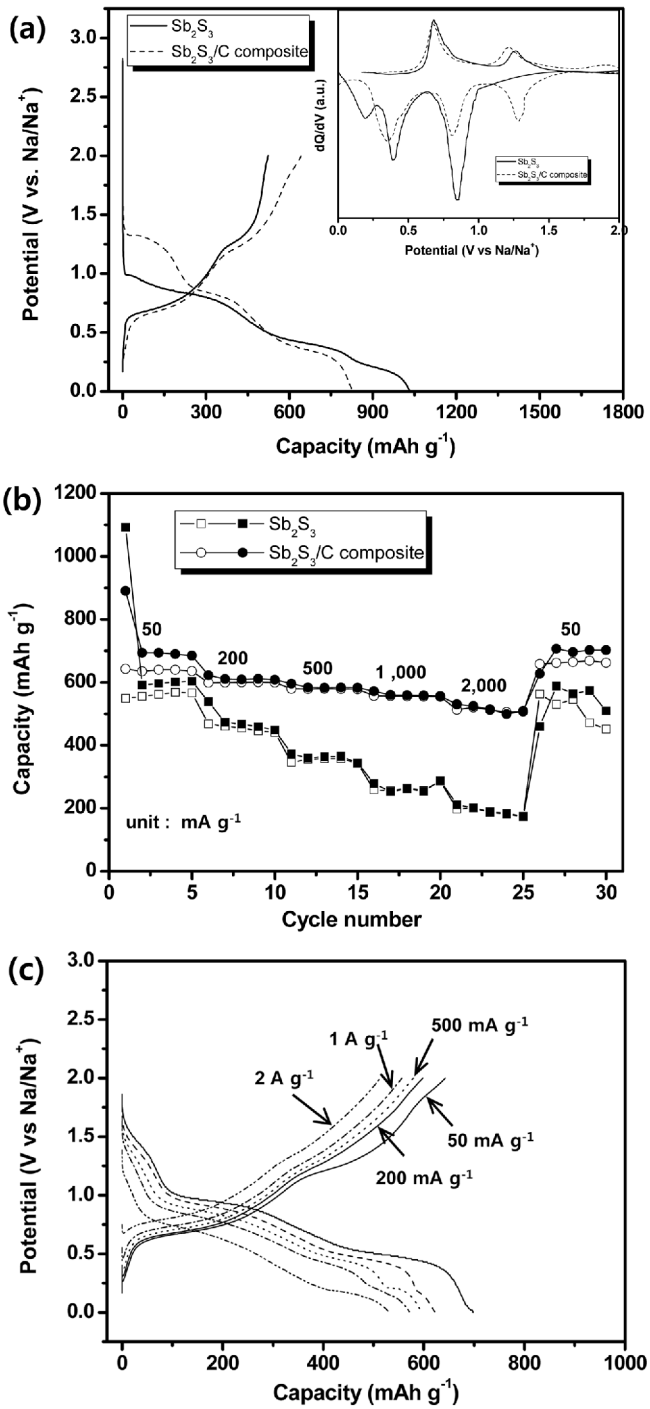

Fig. 3. (a) Initial charge-discharge profiles at 50 mA g^{-1} and (in the inset) DCP curves, (b) rate capabilities of Sb_2S_3 and the Sb_2S_3/C composite, and (c) charge-discharge patterns of the Sb_2S_3/C composite at various current densities.

In addition to a high rate performance, the Sb_2S_3/C composite

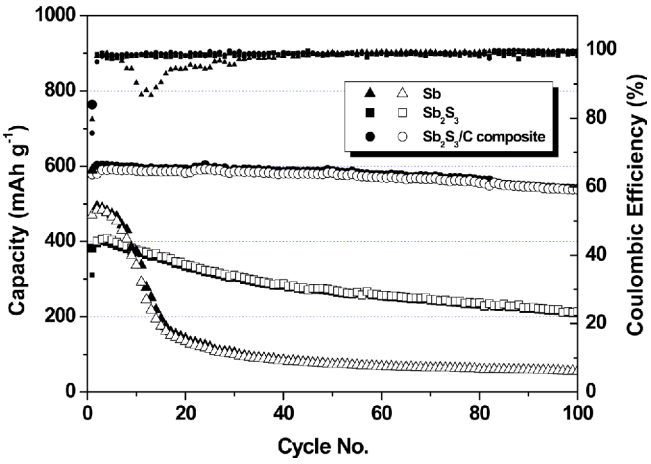

Fig. 4. The cycle performances of the Sb, Sb_2S_3, and Sb_2S_3/C electrodes at 200 mA g^{-1}.

also exhibits good cycling stability. Figure 4 shows the cycling performances of Sb, Sb_2S_3, and the Sb_2S_3 composite with carbon at a current density of 200 mA g^{-1} and their coulombic efficiencies over 100 cycles. The desodiation capacities of Sb, Sb_2S_3, and the Sb_2S_3/C composite after the 100th cycle are 55, 208, and 538 mAh g^{-1}, which correspond to capacity retentions of 11.7%, 52.5%, and 93.1%, respectively. The cycle performances of the three samples are significantly different. The Sb_2S_3 composite with carbon has a superior cycling performance as an anode in NIBs due to the Sb_2S_3 crystallites within the amorphous carbon matrix. In contrast with the outstanding electrochemical performance of the Sb_2S_3/C composite, Sb and Sb_2S_3 exhibit much poorer performances. After the second cycle, the coulombic efficiency of Sb_2S_3/C stabilizes and retains over 99% of this efficiency in the following cycles. This high coulombic efficiency means that this composite can be used as an effective anode material by making the full cell with the cathode material for real applications. The superior rate capability and cycling performance of the Sb_2S_3/C composite indicate that it has good kinetic properties at high current densities and that it retains its structural stability during repeated charge and discharge reactions.

To assess the changes in the Sb_2S_3/C electrode morphology after 100 cycles, SEM images of fresh and 100-cycled electrodes were obtained. Figures 5(a) and 5(b) show that after 100 cycles the Sb_2S_3/C electrode does not crumble, crack, or fragment despite repeated sodiation/desodiation. In addition, the surface of the Sb_2S_3/C electrode is covered with a thin and stable SEI film, which enhances its stability. The photograph confirms that the Sb_2S_3/C electrode retains its structural stability after 100 cycles without electrode pulverization or detachment from the current collector (Fig. 5(c)). As shown in Fig. 5(d), there are no significant differences between the XRD patterns of the fresh and cycled electrodes, i.e. after 100 cycles the electrode retains the structure of the fresh electrode without forming by-products due to side reactions.

In order to understand the electrochemical reaction behavior of the Sb_2S_3/C composite, DCP curves were obtained in the first and second cycles during sodiation/desodiation (Fig.

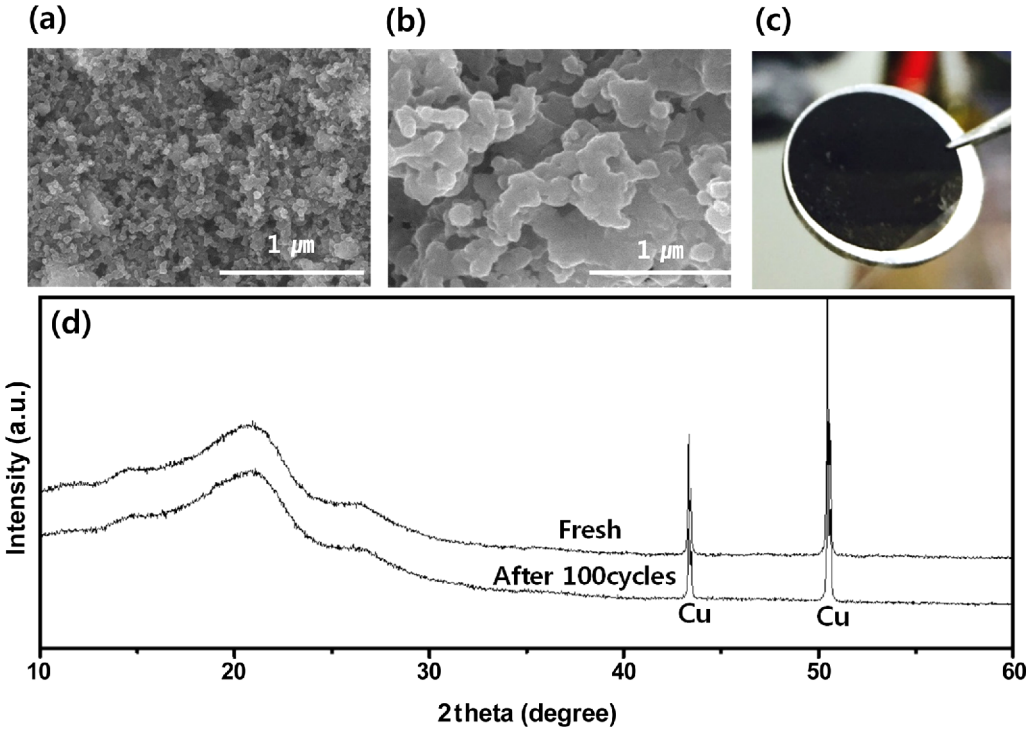

Fig. 5. SEM images; (a) a fresh Sb_2S_3/C electrode and (b) a Sb_2S_3/C electrode after 100 cycles. (c) Photograph of the 100-cycled electrode, and (d) XRD patterns of fresh and 100-cycled electrodes.

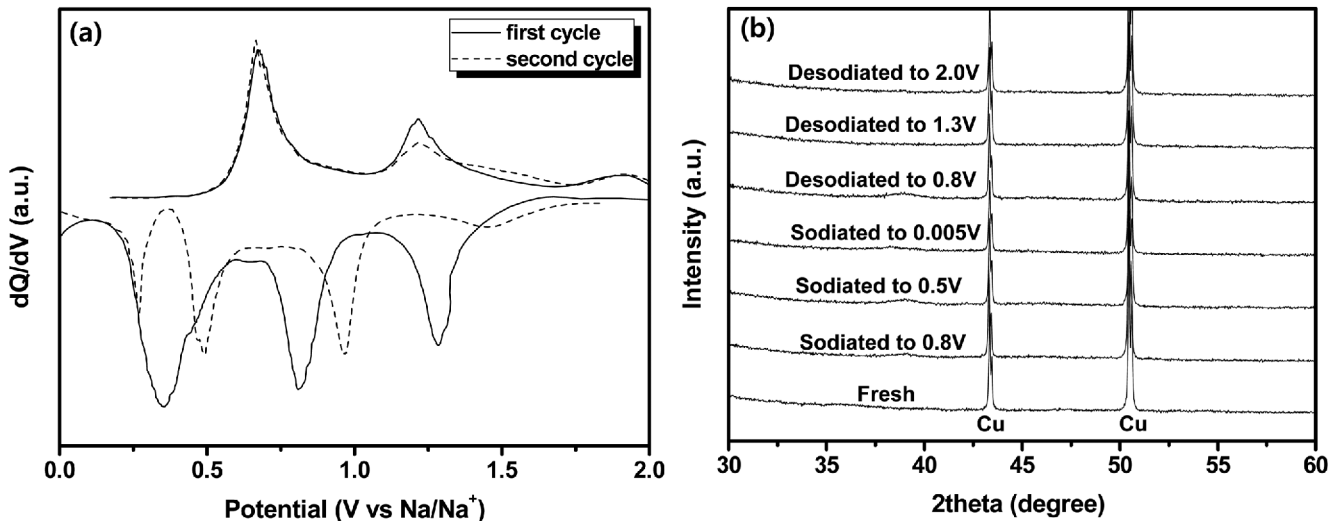

Fig. 6. (a) DCP curves of the Sb_2S_3/C composite in the first and second cycles and (b) XRD patterns with several voltage steps in the first cycle.

6(a)). The sodiation/desodiation profiles of the Sb_2S_3/C composite electrode during the first cycle are obviously different from those of the second cycle, which suggests that stabilization of the electrode surface occurs during the sodiation step in the first cycle. Three reduction peaks are evident at 0.34, 0.81, and 1.28 V during the first cycle, which correspond to electrochemical reduction reactions and SEI formation. The peaks at 0.34 V and 0.81 V correspond to the electrochemical alloying reaction with Sb and S, respectively. The reduction peak at 1.28 V, meanwhile, can be ascribed to the electrolyte decomposition and SEI formation. During the second cycle, reduction peaks can be seen at 0.25, 0.47, and 0.95 V and oxidation peaks at 0.68 and 1.21 V. The potential pair at 0.95/1.21 V is attributed to the alloying/dealloying reactions of elemental S with Na. The reduction and oxidation potentials at 0.25/0.47 and 0.68 V are in good agreement with the results for the alloying/dealloying reactions of Sb with Na reported in a previous study [27].

Based on the voltage profile and DCP curve of the Sb_2S_3/C composite in Fig. 6(a), ex-situ XRD analyses of the electrode were performed at various selected potentials in the first cycle (Fig. 6(b)). Before the reaction with Na, the fresh electrode has an amorphous structure and produces no characteristic crystalline peak. Although this amorphous Sb_2S_3/C composite electrode was sodiated and desodiated to the selected potentials based on the DCP, no crystalline phases became evident during the electrochemical reactions, which suggests that the reaction of this composite with Na may make progress without forming the new crystalline phase during sodiation and desodiation while maintaining short-range ordering. In order to confirm the recombination of Sb and S to reform the original Sb_2S_3 phase, ex-situ HR-TEM analyses were performed at the fully sodiated and desodiated potentials of Sb_2S_3/C composite electrode. At the fully sodiated potential (0.005V vs Na/Na^+, Fig. 7(a)), nanocrystallites of Na_3Sb and Na_2S phases with several nanometers are observed, which demonstrates that Sb_2S_3/C composite is converted to the Na_3Sb and Na_2S phases through conversion reaction during sodiation step. On the other hand, at the fully desodated potential (2.0V vs Na/Na^+, Fig. 7(b)), only Sb_2S_3 phase was detected, which confirms that sodiated phases of Na_3Sb and Na_2S returned to Sb_2S_3 through recombination reaction during desodiation step. The DCP peaks in the first and second cycles also support the conversion and recombination reaction of Sb_2S_3/C composite. The DCP peaks and ex-situ HR-TEM analyses of Sb_2S_3/C electrode at fully sodiated and desodiated potentials suggest that the reactions accompanying the first sodiation and desodiation are as follows:

During sodiation:
$Sb_2S_3 \rightarrow Na_2S + Sb \rightarrow Na_2S + Na_3Sb$
During desodiation:
$Na_2S + Na_3Sb \rightarrow Na_2S + Sb \rightarrow Sb_2S_3$

The conversion and recombination reactions, to which both Sb and S contribute capacity, exhibit high reversible capacity and superior electrochemical performance due to the composite form with carbon.

To interpret the differences between the electrochemical performances of Sb_2S_3 and the Sb_2S_3/C composite, electrochemical impedance spectroscopy (EIS) was conducted on both electrodes after desodiation to 2.0 V in the first cycle. As shown in Fig. 8(a), both electrodes produce similar EIS spectra that are composed of two depressed semicircles and a sloping line. The semicircles are known to be due to the resistance of the SEI film (R_{SEI}) and the charge-transfer resistance (R_{ct}) in the high and low frequency range, whereas the sloping line is associated with sodium-ion diffusion within the bulk of the electrode [28]. Obviously, the two semicircles of the Sb_2S_3/C

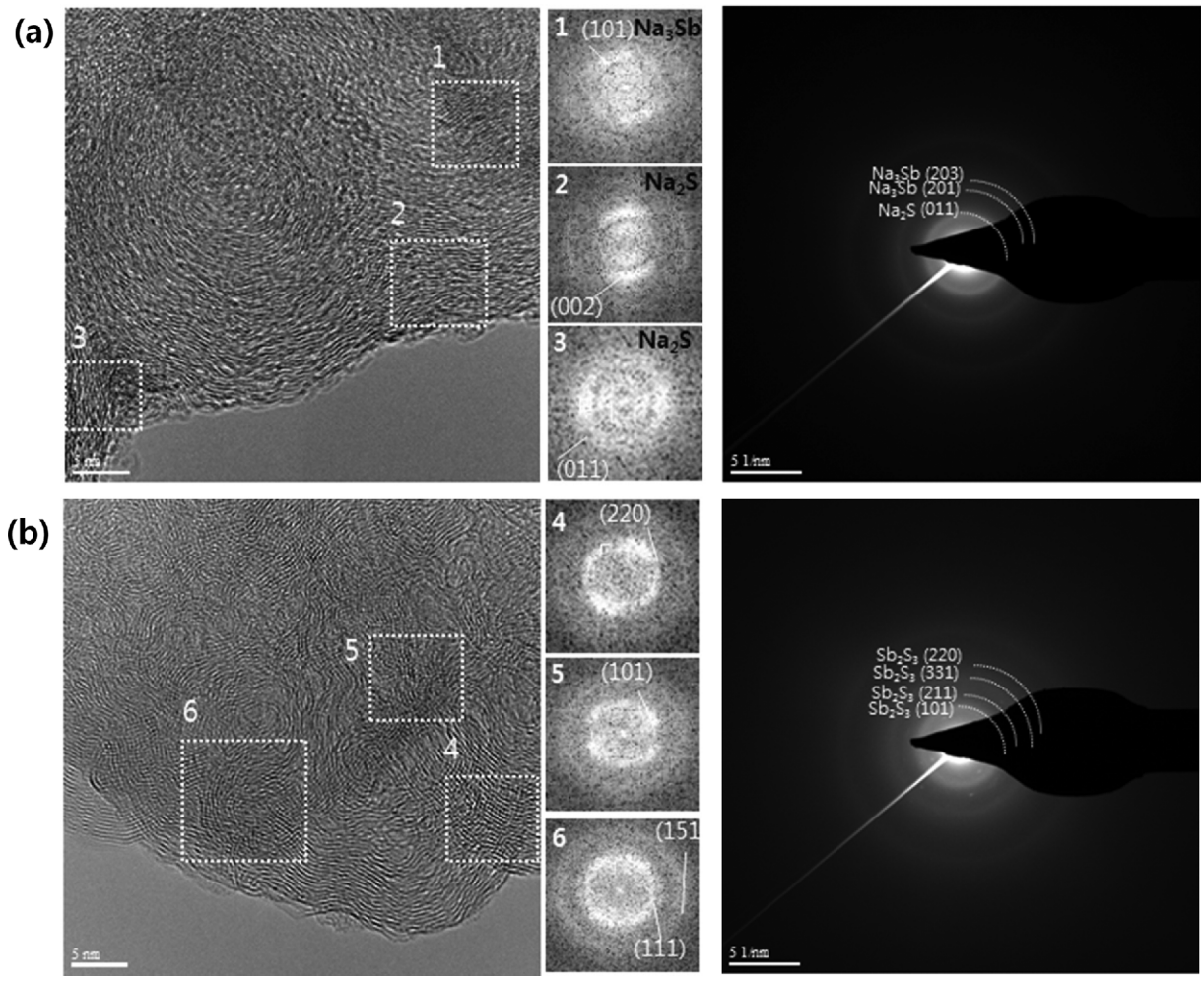

Fig. 7. Ex-situ HR-TEM images with corresponding FT patterns of (a) the fully sodiated and (b) desodiated Sb_2S_3/C composite in the first cycle.

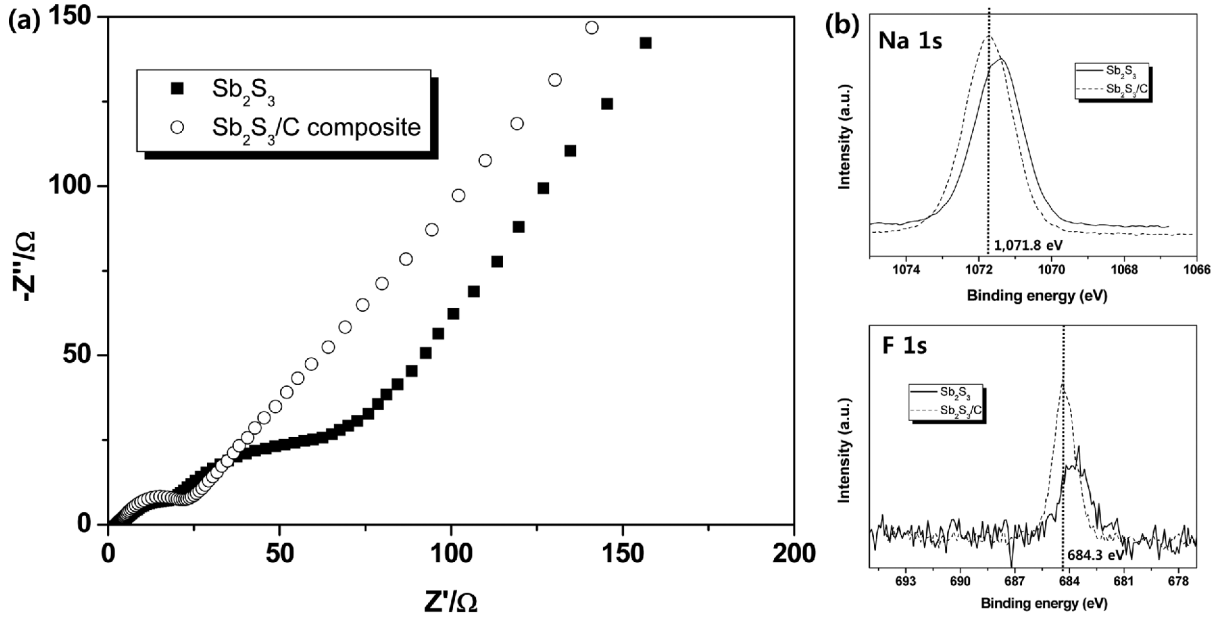

Fig. 8. (a) EIS and (b) XPS spectra of desodiated Sb_2S_3 and Sb_2S_3/C composite in the first cycle.

composite anode are much smaller than those of Sb_2S_3, which indicates that the R_{SEI} and R_{ct} values of the Sb_2S_3/C composite are reduced owing to coated carbon on the Sb_2S_3 surface. These reductions of the surface film resistance and the charge transfer resistance due to carbon's conducting and buffering effects result in the enhancement of the electrochemical properties. Therefore, the EIS study confirms that the preparation with HEMM of a composite of Sb_2S_3 and carbon is effective in improving the interfacial kinetic properties of the Na ions and electrons, which results in an NIB anode material with superior electrochemical performance.

In order to better understand the effects of the SEI layer on the performance of Sb_2S_3 and Sb_2S_3/C electrodes, XPS analyses are conducted on both electrodes at the fully desodiated electrodes (Fig. 8(b)). For the Sb_2S_3/C electrodes, the formation of compact NaF film is suggested by the Na1s spectra at 1,071.8 eV and the F1s spectra at 684.3 eV. On the other hand, Sb_2S_3 electrode has the lower peak intensity of F1s spectra corresponding to NaF, indicating that the stable NaF layer is not formed on Sb_2S_3 electrode. Therefore, the formation and presence of compact and stable NaF layer during the sodiation/desodiation reaction, can help Sb_2S_3/C electrode achieve the superior electrochemical performances [29,30].

Figure 9 shows the voltage profiles and the changes in thickness of the electrodes during sodiation and desodiation. After the electrode was fully sodiated and desodiated, the thickness of each electrode in the disassembled cell was measured with a micrometer at state of charge (SOC) values of 0% and 100%. The thickness of the Sb_2S_3/C composite electrode increases by only 74% in the fully sodiated state, which is less than those of Sb (196%) and Sb_2S_3 (107%). Although the Sb_2S_3 and Sb_2S_3/C electrodes have higher sodiation capacities than elemental Sb, their degrees of swelling are much lower than that of Sb. Thus S and carbon in Sb_2S_3 and the Sb_2S_3/C composite provide a buffering matrix that accommodates volume expansion during sodiation/desodiation. The swelling properties of the Sb_2S_3/C composite electrode are also much superior to those of

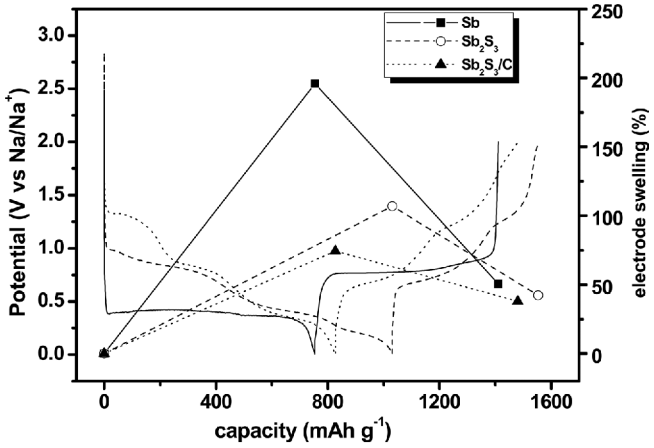

Fig. 9. Charge-discharge patterns and changes in thickness of the Sb, Sb_2S_3, and Sb_2S_3/C electrodes in the first cycle.

a previously reported phosphorus/carbon composite (187%) [31]. The thickness at SOC 0% of the electrode, which is fully desodiated at 2.0 V vs. Na/Na^+, is almost recovered to that of the fresh electrode, with a small expansion of only 27%. Although the expansion of the Sb_2S_3/C composite electrode is less than those of the other materials (Sb, P/C), its degree of swelling is still not adequate given that the acceptable degree of thickness change for practical applications is approximately 30% [32]. Therefore, further study of the control of changes in the thickness of the electrode during sodiation and desodiation is necessary.

4. CONCLUSION

Sb_2S_3/carbon composites are successfully synthesized with a facile mechanochemical method and their electrochemical performances as anodes in sodium ion batteries are investigated. It is found that the Sb_2S_3 composite with carbon exhibits better electrochemical performance, including a high reversible capacity of 654 mAh g^{-1}, a high initial coulombic efficiency of 78% that surpasses the results of previous studies of Sb_2S_3, and an excellent cycling performance with a residual capacity ratio of 93.1% over 100 cycles. Furthermore, it shows a good rate capability, i.e. a high desodiation capacity of 526 mAh g^{-1} at 2,000 mA g^{-1} corresponding to 3C rate. This material also exhibits much less swelling (74%) at the fully sodiated state, comparing with Sb or Sb_2S_3. These outstanding results for the Sb_2S_3/C composite are attributed to the following factors: (1) both Sb and S react with Na, which provides high capacity, (2) the buffering effects of Sb and S through the formation of Na-Sb and Na-S phases with different reaction potentials, and (3) the improvement in the interfacial conductivity that results from the carbonaceous surface on the anode. XPS and EIS analyses also confirm that the compact NaF inorganic passivation film is formed on the carbonaceous surface of Sb_2S_3/C composite during electrochemical reaction, leading to much lower charge transfer and SEI resistance than Sb_2S_3. In addition, we have elucidated a reactions mechanism during sodiation and desodiation by performing ex-situ XRD and DCP analyses. As discussed above, the electrochemical performances of bulky modified Sb_2S_3 anode can be maximized with tailored artificial interface via intentionally composing carbonaceous surface, and thus considered as a promising anode material for sodium ion batteries.

ACKNOWLEDGMENT

This research was supported by the Korea Electrotechnology Research Institute (KERI) Primary Research Program through the National Research Council of Science & Technology funded by the Ministry of Science, ICT and Future Planning (MSIP) (No. 16-12-N0101-20) and by the Korea Institute of Energy Technology Evaluation and Planning (KETEP) and the Ministry of Trade, Industry & Energy (MOTIE) of the Republic of Korea (No. 20152020105420).

REFERENCES

1. M. Armand and J. M. Tarascon, *Nature* **451**, 652 (2008).
2. P. G. Bruce, B. Scrosati, and J. M. Tarascon, *Angew. Chem. Int. Edit.* **47**, 2930 (2008).
3. J. M. Tarascon and M. Armand, *Nature* **414**, 359 (2001).
4. B. Dunn, H. Kamath, and J. M. Tarascon, *Science* **334**, 928 (2012).
5. Z. Yang, J. Zhang, M. Kintner-Meyer, X. Lu, D. Choi, J P. Lemmon, *et al. Chem. Rev.* **111**, 3577 (2011).
6. C.-M. Park, J.-H. Kim, H. Kim, and H.-J. Sohn, *Chem. Soc. Rev.* **39**, 3115 (2010).
7. B. Scrosati and J. Garche, *J. Power Sources* **195**, 2419 (2010).
8. M. S. Whittingham, *Chem. Rev.* **104**, 4271 (2004).
9. C. Grosjean , P. H. Miranda, M. Perrin, and P. Poggi, *Renew. Sust. Energ. Rev.* **16**, 1735 (2012).
10. N. Yabuuchi, K. Kubota, M. Dahbi, and S. Komaba, *Chem. Rev.* **114**, 11636 (2014).
11. M. D. Slater, D. Kim, E. Lee, and C. S. Johnson, *Adv. Funct. Mater.* **23**, 947 (2013).
12. N. Yabuuchi, M. Kajiyama, J. Iwatate, H. Nishikawa, S. Hitomi, S. Komaba, *et al. Nat. Mater.* **11**, 512 (2012).
13. S. W. Kim, D. H. Seo, X. Ma, G. Ceder, and K. Kang, *Adv. Energy Mater.* **2**, 710 (2012).
14. S. Y. Hong, Y. Kim, Y. Park, A. Choi, N.-S. Choi, and K. T. Lee, *Energ. Environ. Sci.* **6**, 2067 (2013).
15. H. Kang, Y. Liu, K. Cao, Y. Zhao, L. Jiao, H. Yuan, *et al. J. Mater. Chem. A* **3**, 17899 (2015).
16. F. Sauvage, L. Laffont, J. M. Tarascon, and E. Baudrin, *Inorg. Chem*. **46**, 3289 (2007).
17. Y. Cao, L. Xiao, M. L. Sushko, W. Wang, B. Schwenzer, J. Liu, *et al. Nano Lett*. **2**, 3783 (2012).
18. M. Dahbi, N. Yabuuchi, K. Kubota, K. Tokiwa, and S. Komaba, *Phys. Chem. Chem. Phys*. **16**, 15007 (2014).
19. J. Qian, X. Wu, Y. Cao, X. Ai, and H. Yang, *Angew. Chem. Int. Ed.* **52**, 4731 (2013).
20. A. Darwiche, C. Marino, M. T. Sougrati, B. Fraisse, L. Stievano, and L. Monconduit, *J. Am. Chem. Soc*. **134**, 20805 (2012).
21. J. Qian, Y. Chem, L. Wu, Y. Cao, X. Ai, and H. Yang, *Chem. Commun*. **48**, 7070 (2012).
22. H. Hou, Y. Yang, Y. Zhu, M. Jing, C. Pan, X. Ji, *et al. Electrochim. Acta* **146**, 328 (2014).
23. L. Wu, X. Hu, J. Qian, F. Pei, F. Wu, Y. Cao, *et al. Energy Environ. Sci.* **7**, 323 (2014).
24. Y. Zhu, X. Han, Y. Xu, Y. Lu, S. Zheng, C. Wang, *et al. ACS Nano.* **7**, 6378 (2013).
25. H. Hou, M. Jing, Y. Yang, Y. Zhang, Y. Zhu, X. Ji, *et al. J. Mater. Chem. A* **3** 2971 (2015).
26. Y. Zhu, P. Nie, L. Shen, S. Dong, Q. Sheng, X. Zhang, *et al. Nanoscale* **7**, 3309 (2015).
27. D. Y. W. Yu, P. V. Prikhodchenko, C. W. Mason, S. K. Batabyal, J. Gun, O. Lev, *et al. Nat. Commun*. **4**, 2922 (2013).
28. H. Lu, L. Wu, L. Xiao, X. Ai, H. Yang, and Y. Cao, *Electrochim. Acta* **190**, 402 (2016).
29. L. Baggetto, P. Ganesh, C.-N. Sun, R. A. Meisner, T. A. Zawodzinski, and G. M. Veith, *J. Mater. Chem. A* **1**, 7985 (2013).
30. L. Bodenes, A. Darwiche, L. Monconduit, and H. Martinez, *J. Power Sources* **273**, 14 (2015).
31. Y. Kim, Y. Park, A. Choi, N.-S. Choi, J. Kim, K. T. Lee, *et al. Adv. Mater*. **25**, 3045 (2013).
32. Y. Kim, Y. Kim, A. Choi, S. Woo, D. Mok, K.T. Lee, *et al. Adv. Mater.* **26**, 4139 (2014).